

Hiding Local Manipulations on SAR Images: a Counter-Forensic Attack

Sara Mandelli, *Member, IEEE*, Edoardo Daniele Cannas, *Student Member, IEEE*, Paolo Bestagini, *Member, IEEE*, Stefano Tebaldini, *Member, IEEE*, and Stefano Tubaro, *Senior Member, IEEE*

Abstract—The vast accessibility of Synthetic Aperture Radar (SAR) images through online portals has propelled the research across various fields. This widespread use and easy availability have unfortunately made SAR data susceptible to malicious alterations, such as local editing applied to the images for inserting or covering the presence of sensitive targets. Vulnerability is further emphasized by the fact that most SAR products, despite their original complex nature, are often released as amplitude-only information, allowing even inexperienced attackers to edit and easily alter the pixel content. To contrast malicious manipulations, in the last years the forensic community has begun to dig into the SAR manipulation issue, proposing detectors that effectively localize the tampering traces in amplitude images. Nonetheless, in this paper we demonstrate that an expert practitioner can exploit the complex nature of SAR data to obscure any signs of manipulation within a locally altered amplitude image. We refer to this approach as a counter-forensic attack. To achieve the concealment of manipulation traces, the attacker can simulate a re-acquisition of the manipulated scene by the SAR system that initially generated the pristine image. In doing so, the attacker can obscure any evidence of manipulation, making it appear as if the image was legitimately produced by the system. We assess the effectiveness of the proposed counter-forensic approach across diverse scenarios, examining various manipulation operations. The obtained results indicate that our devised attack successfully eliminates traces of manipulation, deceiving even the most advanced forensic detectors.

Index Terms—SAR Images, Speckle Noise, Image Manipulation Detection, Image Manipulation Localization, SAR Forensics.

I. INTRODUCTION

Synthetic Aperture Radar (SAR) images are remote sensing data that use radar waves to create two-dimensional or three-dimensional representations of objects or landscapes. Over the last years, many online portals have given access to SAR images in easy-to-download and manageable data products.

Authors are with the Dipartimento Elettronica, Informazione e Bioingegneria - Politecnico di Milano - Milan, Italy (email: name.surname@polimi.it).

This material is based on research sponsored by the Defense Advanced Research Projects Agency (DARPA) and the Air Force Research Laboratory (AFRL) under agreement number FA8750-20-2-1004. The U.S. Government is authorized to reproduce and distribute reprints for Governmental purposes notwithstanding any copyright notation thereon. The views and conclusions contained herein are those of the authors and should not be interpreted as necessarily representing the official policies or endorsements, either expressed or implied, of DARPA and AFRL or the U.S. Government. This work was partially supported by the European Union under the Italian National Recovery and Resilience Plan (NRRP) of NextGenerationEU, partnership on “Telecommunications of the Future” (PE00000001 - program “RESTART”). This work has been also partially supported by SERICS (PE00000014) under the MUR National Recovery and Resilience Plan funded by the European Union – NextGenerationEU. This work was also supported by the FOSTERER project, funded by the Italian Ministry of University, and Research within the PRIN 2022 program.

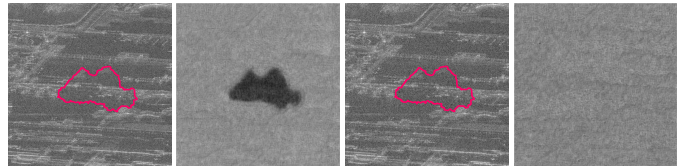


Fig. 1: High-level description of the paper goal. Given a manipulated SAR amplitude image (left), state-of-the-art SAR forensic detectors estimate a fingerprint (second column) that highlights local image inconsistencies. Our proposed counter-forensic attack simulates a SAR re-acquisition of the manipulated image. The attack leaves untouched the semantic content of the image (third column), but it conceals its tampering traces, such that the estimated fingerprint (right) does not allow anymore to localize the forgery. The manipulation area is surrounded by the red contour.

Among these portals, we can find the European Space Agency (ESA) Copernicus Open Access Hub [1], ICEYE [2] and Capella [3]. This phenomenon bolstered the research in the SAR field, with various applications in geology, hydrology, forestry, agriculture, urban planning, disaster management, intelligence, and military investigations [4], [5]. For example, SAR data can localize sensitive targets like army vehicles [6], ships [7], airports [8] and aircrafts [9].

Unfortunately, the vast popularity of SAR images and the presence of easy-to-manage products make them a target for malicious manipulations. Despite these images being complex signals, most SAR data products only provide amplitude information, i.e., they report information as a real-valued data matrix. An attacker, even an inexperienced one, can open these images, edit them with a common editing software and alter their content [10]. For instance, inserting or covering the presence of military vehicles is becoming a relatively easy task and has the potential of carrying severe consequences in the context of ground monitoring analysis.

For this reason, SAR images are becoming objects of investigation by the multimedia forensic community [11], [10], [12]. Given the particular processing pipeline of SAR images, researchers have developed techniques tailored explicitly to them [11], proposing solutions for the localization of tampered-with pixel regions [10]. In particular, the authors of [10] have proposed a SAR forensic detector that uncovers traces of manipulations applied locally on SAR amplitude images. Given a SAR amplitude image, the detector processes it to estimate a fingerprint map that highlights local inconsistencies. If the map is homogeneous, the image is likely pristine; if the map shows a region with completely different characteristics than the rest, the image has been likely manipulated within that area. An example of the fingerprint returned by this detector is shown in Fig. 1. Given a manipulated image

(left), the detector is able to localize the tampering area with high accuracy (second column).

So far, the forensic community has worked considering the amplitude information of SAR signals exclusively. However, SAR signals are naturally complex, i.e., they report both amplitude and phase. Phase information is crucial in specific applications, such as interferometry [4], and makes SAR images sensibly different from standard digital photographs or other modalities of remote sensing data. These differences emerge in the acquisition pipeline of SAR data and some unique degradation phenomena that afflict it [13], [10]. One is speckle noise, i.e., the coherent interference of the scattered waves from multiple targets within a resolution cell [14].

In this work, we prove that an experienced practitioner can exploit the complex nature of SAR data to conceal the manipulation traces from a locally manipulated SAR amplitude image. If any information on the SAR satellite used to acquire the original image is available, it can be used to simulate a complete re-acquisition of the manipulated scene. In doing so, we show that it is possible to produce an image with the same semantic content of the manipulated one, but with similar SAR characteristics to pristine ones, where the tampering traces have been hidden. A high-level example of the tackled goal is shown in Fig. 1. Given a manipulated amplitude SAR image (left), we produce a modified version of it (third column) such that the fingerprint estimated by the forensic detector does not highlight the forgery, but resembles that of a pristine image, hiding the manipulation artifacts (right).

The forensic community refers to this kind of operation as a counter-forensic attack. The goal of such attacks is usually twofold. On the one hand, the attack simulates the scenario in which a user produces a manipulation and is able to hinder the traces left by the tampering process. Notice that this does not involve malicious intents only; indeed, it can answer to privacy preserving needs in case specific image manipulations are inserted to hide sensitive targets. In this scenario, the attack allows to avoid the manipulation traces to be exposed. On the other hand, the attack allows to test the robustness of existing forensic detectors in spotting the manipulation even in presence of counter-forensic operations.

In our proposed counter-forensic attack, we alter the amplitude component of a complex SAR product, and we show that we are able to conceal the forensic footprints left by the manipulation by modeling the SAR acquisition and processing system with different strategies. In particular, we build a dataset of manipulated SAR amplitude images and validate the proposed pipeline in various scenarios, considering different manipulation operations and investigating in depth the effect of our methodology on their traces.

The achieved results show that the proposed attack wipes out the manipulation traces, fooling the most advanced forensic detectors. Moreover, the produced images carry typical SAR characteristics similar to original pristine ones, such that even an expert SAR analyst would not be able to realize the difference with the original data.

To summarize, our contributions are the following:

- We propose a counter-forensic attack that, leveraging the complex nature of SAR data, can fool advanced forensic

detectors designed for SAR amplitude images.

- The proposed attack enables to simulate scenarios in which a malicious user wants to delete their traces, but it allows as well to preserve the privacy in case sensitive targets must be hidden from the depicted scene.
- The proposed attack enables to test the robustness and weaknesses of the existing forensic detectors in case of malicious attacks.
- The manipulated images that undergo our proposed attack maintain similar characteristics than pristine data for what concerns their visual quality, SAR properties and frequency behaviour, thus rendering the attack difficult to be spot by expert researchers in the field.
- We validate the proposed pipeline on a dataset of automatically spliced SAR images, but we also experiment on hand-made forgeries that resemble realistic and potentially alarming scenarios.

II. BACKGROUND

In this section, we present some background concepts useful to understand the tackled objective and the proposed methodology. We start reporting details on SAR imaging; then, we show the most common SAR image manipulations; finally, we describe the existing state-of-the-art forensic detectors that deal with such manipulations.

A. SAR Imaging

A SAR system involves an imaging radar installed on a mobile platform, such as a satellite or an aircraft, moving in a specific direction. As it moves, the system transmits a series of high-power electromagnetic waves through its antenna. These waves engage with the objects they encounter on the Earth's surface and undergo backscattering, altering their amplitude and phase based on the permittivity and physical characteristics of the objects, like geometry and roughness. Subsequently, the antenna captures these modified echoes, which can be processed to generate the complex SAR image [13].

This final image can undergo additional processing. According to the specific acquisition mode and type of additional processing applied, various distinct SAR products can be generated [15]. For instance, SAR images can be acquired with Strip, Spot and Scan acquisition modes [16], which results in images with different spatial resolution and spectral features. Then, SAR images can be processed to obtain Single Look Complex (SLC), Multi Look Complex (MLC) or Ground Range Detected (GRD) products. Among them, SLC processing considers a single acquisition step per scene, retaining full resolution in azimuth and range directions. SLC images have the highest fidelity of all SAR image products, as they are free from interpolation or projection artifacts. For this reason, SLC products are usually employed for SAR quality assessment, calibration and interferometric applications [17].

In the next lines, we first describe the general end-to-end SAR system model, which refers to the entire pipeline of data acquisition and formation. Then, we provide some details on speckle noise, which characterizes all SAR imaging systems.

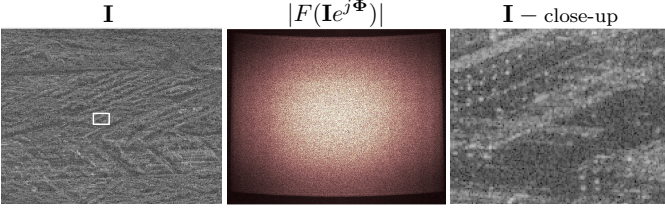


Fig. 2: Example of 2D SLC SAR image $\mathbf{I}e^{j\Phi}$. First, we report the amplitude component \mathbf{I} ; then, the amplitude of the FT of the complex image $F(\mathbf{I}e^{j\Phi})$; finally, the close-up of \mathbf{I} in the pixel area surrounded by the white box.

1) *End-to-end SAR system model*: The end-to-end SAR system model regards the modeling of the entire process which starts from the reflection from a scattering object until its conversion into an image. The process starts from the source complex scene reflectivity, which collects all the information regarding the object's characteristics (like permittivity, conductivity and surface structure) and the antenna system (e.g., the wavelength of transmitted waves, the polarization, the incidence angle and the imaging geometry) [13]. Focusing on SAR 2D imagery, we can model a generic scene reflectivity image as $\mathbf{I}_R e^{j\Phi_R}$, where $\mathbf{I}_R \in \mathbb{R}^{X \times Y}$ is the amplitude component and $\Phi_R \in \mathbb{R}^{X \times Y}$ is the phase term. X and Y correspond to range (i.e., the direction perpendicular to platform flight along which the electromagnetic beam travels) and azimuth (the actual trajectory of the platform), respectively.

The scene reflectivity is acquired by the SAR system in the form of backscattered echoes, which are usually denoted as raw data. The process that regresses raw data back to an estimate of the complex reflectivity scene is named focusing, or image formation. In the SAR imaging community, it is common to model the entire acquisition and processing chain as a cascade of linear filters [13], [18], [19]. The final image spectrum can be related to the initial scene reflectivity spectrum as

$$F(\mathbf{I}e^{j\Phi}) = F(\mathbf{I}_R e^{j\Phi_R}) \odot \mathbf{H}(f_x, f_y), \quad (1)$$

where the operator $F(\cdot)$ describes the 2D Fourier Transform (FT) and \odot describes the element-wise product, while $\mathbf{H}(f_x, f_y)$ is the 2D transfer function of the end-to-end SAR system model, expressed as a function of the spatial frequencies f_x and f_y . The final 2D image $\mathbf{I}e^{j\Phi} \in \mathbb{C}^{X \times Y}$ is the result of the SAR acquisition and focusing operations. An example of the amplitude of a 2D SLC SAR image selected from the TerraSAR-X ESA archive [20] is reported in Fig. 2 (left).

In particular, for spaceborne strip-map data $\mathbf{H}(f_x, f_y)$ can be described as a linear azimuth and range invariant operator, which is usually approximated as a non-negative real central-symmetric 2D filter with a low pass behaviour [13], [19]. Formally,

$$\begin{aligned} \mathbf{H}(f_x, f_y) &\geq 0; \\ \mathbf{H}(-f_x, -f_y) &= \mathbf{H}(f_x, f_y); \\ \mathbf{H}(f_x, f_y) &\approx 0, \quad \forall |f_x| > f_{c_x}, \forall |f_y| > f_{c_y}, \end{aligned} \quad (2)$$

being f_{c_x}, f_{c_y} specific cutoff frequencies along azimuth and range dimensions, respectively. These frequencies may be known in advance if the SAR system model is known, but they can be easily inferred by observing the spectrum of

the final image $\mathbf{I}e^{j\Phi}$ [19]. Fig. 2 (center) reports the magnitude spectrum of the previously referred SAR image. It is noticeable the low pass behaviour along both frequency dimensions, though the spectrum is very wide; moreover, in correspondence of horizontal and vertical cutoff frequencies, the magnitude shows a steep drop towards the zero.

2) *Speckle pattern*: In the SAR imaging community, it is well-known that the majority of surfaces exhibit significant roughness at the scale of an optical wavelength [14]. When exposed to coherent radiation, the wave reflected from such surfaces comprises contributions from numerous independent scattering areas with various different relative delays. The inference of these contributions gives rise to a typical granular pattern known as speckle [14]. This pattern typically presents a continuum of irradiance values, which range from dark spots (due to destructive interference) to bright spots (due to constructive interference).

The statistical modeling of the speckle pattern is done by considering the sum of the various complex microscopic contributions. Each component carries an amplitude and a phase that are statistically independent of each other and of the amplitude and phase of the other components [14]. Given a large number of contributions, it can be proved that the speckle pattern components (the real and the imaginary part) are independent and identically distributed as a Gaussian probability density function with zero mean. This results in a complex speckle pattern $\mathbf{S}e^{j\Phi_S}$ with an amplitude $\mathbf{S}(x, y)$ characterized by a Rayleigh probability density function and a phase term $\Phi_S(x, y)$ uniformly distributed [21]. More specifically, $\mathbf{S}(x, y) \sim \mathcal{R}(\sigma_S)$, being σ_S the scale parameter of a Rayleigh probability distribution, whether $\Phi_S(x, y) \sim \mathcal{U}[0, 2\pi]$.

If we restrict the field to SLC SAR images (i.e., when a single image of the scene reflectivity is acquired and processed by the SAR system), the scene reflectivity $\mathbf{I}_R e^{j\Phi_R}$ (i.e., the source data that enters the SAR imaging system) follows a multiplicative speckle model with a fully developed speckle [22]. In practice, $\mathbf{I}_R e^{j\Phi_R}$ results from the element-wise product of a hypothetically noise-free image $\mathbf{I}_0 e^{j\Phi_0}$ (which can be seen as a non-observable signal in our model), and the speckle pattern. Thus, $\mathbf{I}_R e^{j\Phi_R} = \mathbf{I}_0 e^{j\Phi_0} \odot \mathbf{S}e^{j\Phi_S}$.

As a consequence, the scene reflectivity image is composed by the contributions of manifold complex components, each due to a different scattering point on the target surface, showing a speckle pattern superimposed to the image of interest [14]. This pattern is maintained throughout the process of SAR data acquisition and focusing, thus it is reflected in the final reconstructed image $\mathbf{I}e^{j\Phi}$. In Fig. 2 (right) we show a close-up of the previously shown 2D SAR amplitude image, which is actually an SLC image thus it reasonably contains a high amount of speckle noise. It is noticeable the effect of the speckle pattern as a granular noise superimposed to the scene of interest.

B. SAR amplitude image manipulations

In this paper we deal with the detection of local manipulations on SLC SAR amplitude images. These images may be manipulated for a variety of reasons, which span from legitimate privacy concerns up to malicious intents guided

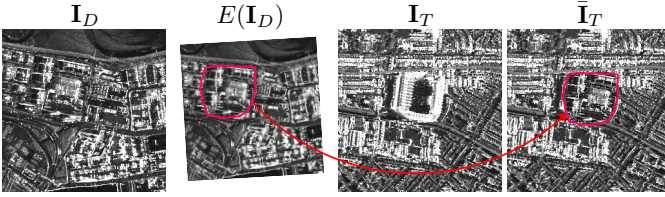


Fig. 3: Example of forgery creation process. From left to right: the donor image \mathbf{I}_D ; the edited version of the donor image $E(\mathbf{I}_D)$; the target image \mathbf{I}_T ; the locally manipulated target image $\bar{\mathbf{I}}_T$. The splicing is performed by copying a region of the edited donor image into the target one. The manipulation area is surrounded by the red contour.

by political reasons or military purposes in war scenarios. As other kinds of digital imagery, these data can be easily manipulated through editing software suites like Photoshop or GIMP, as well as through synthetic generation tools [23], [24].

Inspired by [10], we can formally describe the forgery creation process of a SAR amplitude image as follows. We define a generic pristine amplitude SAR image as \mathbf{I} , with size $X \times Y$. Let \mathbf{I}_D and \mathbf{I}_T be two pristine SAR amplitude images; \mathbf{I}_D is the donor image, whereas \mathbf{I}_T is the target one. We define $\bar{\mathbf{I}}_T$ as the tampered with version of \mathbf{I}_T , which has been locally manipulated by splicing a specific pixel area of \mathbf{I}_D into \mathbf{I}_T .

As done in [10], we acknowledge the possibility that, before the splicing, the pixels of the donor image might have undergone additional editing procedures like resizing, rotation or noise addition to enhance the credibility and visual appeal of the attack. For example, rotation and resizing could be necessary to align the content of the source and target images and prevent the splicing from being easily detectable upon visual inspection. Therefore, we define the generic edited version of the donor image as $E(\mathbf{I}_D)$, with $E(\cdot)$ being a suitable editing function. We define the donor pixel region of $E(\mathbf{I}_D)$ as \mathcal{D} and the target pixel region of \mathbf{I}_T as \mathcal{T} . \mathcal{T} is the region of \mathbf{I}_T under splicing attack. \mathcal{D} and \mathcal{T} are congruent, i.e., the two pixels' regions have the same shape, size and orientation. They can differ in their location inside the respective images $E(\mathbf{I}_D)$ and \mathbf{I}_T . Fig. 3 provides an example of splicing operation. The original target amplitude image \mathbf{I}_T depicts a strong scatterer in the middle area. This region can be hidden by splicing a portion of the donor amplitude image \mathbf{I}_D into \mathbf{I}_T , after the application of little downscaling and rotation to match the dimensions.

We formally define the resulting spliced image $\bar{\mathbf{I}}_T$ as:

$$\bar{\mathbf{I}}_T(x, y) = \begin{cases} \mathcal{D}(x', y') & \text{if } (x, y) \in \mathcal{T} \\ \mathbf{I}_T(x, y), & \text{if } (x, y) \notin \mathcal{T} \end{cases}, \quad (3)$$

being (x', y') the point coordinates of the donor region corresponding to the target coordinates (x, y) .

The splicing operation can be described by a tampering mask \mathbf{M} , with the same size of \mathbf{I}_T , where each pixel takes a binary value 0 or 1 depending on the pixel of $\bar{\mathbf{I}}_T$ being pristine or manipulated, respectively. Formally, the tampering mask \mathbf{M} has pixel values equal to

$$\mathbf{M}(x, y) = \begin{cases} 1, & \text{if } (x, y) \in \mathcal{T} \\ 0, & \text{if } (x, y) \notin \mathcal{T} \end{cases}. \quad (4)$$

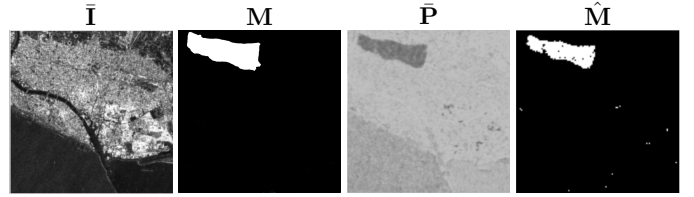


Fig. 4: Example of fingerprint $\bar{\mathbf{P}}$ and estimated tampering mask $\hat{\mathbf{M}}$ extracted by the detection method proposed in [10] from a spliced amplitude image $\bar{\mathbf{I}}$. The precise location of the spliced pixel area is reported in \mathbf{M} .

C. SAR forensic detectors

The forensic community has developed manifold image splicing detectors during the years, specifically focused on classic 8-bit imagery like photographs or video frames [25], [26]. All the deployed detectors leverage the same assumption, that is, the acquisition device and processing operations leave peculiar traces on images, and these can be exploited to expose local forgeries [27], [26].

The acquisition pipeline of SAR amplitude images is completely different than digital photographs or video sequences. Nonetheless, it has been shown that different SAR products reasonably contain different traces relative to the processing executed for generating them [10]. In this vein, the authors of [10] recently proposed a forensic detector for localizing splicing areas on SAR amplitude images. This detector highlights local inconsistencies between the donor and target pixel areas, and proves superior than state-of-the-art detectors on these specific images.

The detector training phase involves a siamese training of a denoising network architecture known as Denoising Convolutional Neural Network (DnCNN) [28]. The training process can be summarized by these three steps:

- 1) Consider a number of SAR amplitude images coming from different products.
- 2) Apply the DnCNN to patches extracted from different images to obtain a series of noise patterns.
- 3) Train the DnCNN to extract similar noise patterns for patches coming from the same product, and different patterns from patches coming from different products.

Eventually, the trained DnCNN is able to extract a noise-like fingerprint with the same size of the input image. This fingerprint contains traces related to the processing pipeline of the acquired product, highlighting potential splicing attacks as traces' inconsistencies. Indeed, when analyzing pristine images, the fingerprint is self-consistent, whereas in case of spliced images it clearly highlights the edited regions.

More formally, let us consider a generic manipulated amplitude image as input to the detector. For simplicity, we omit the subscript T from the manipulated images notation, taking for granted that all amplitude images indicated as $\bar{\mathbf{I}}$ have been manipulated in a specific target region of pixels, identified by the tampering mask \mathbf{M} . At first stage, the detector estimates a real-valued fingerprint map $\bar{\mathbf{P}}$, exposing local inconsistencies between pixels. Given $\bar{\mathbf{P}}$, the authors propose different methods to process $\bar{\mathbf{P}}$ for estimating a binary mask $\hat{\mathbf{M}}$ that identifies the forgery region. For an extensive description of the method, we refer the interested reader to [10].

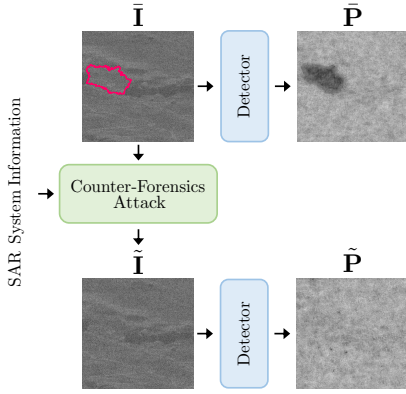


Fig. 5: Sketch of the tackled counter-forensic task. Given a manipulated amplitude image \bar{I} and some information on the SAR system used to acquire the original data, we aim at producing an amplitude image \tilde{I} in which the manipulation traces have been concealed.

Fig. 4 shows an example of fingerprint and tampering mask estimated by the detector. Notice that the splicing area is easily recognizable even from the fingerprint \bar{P} . In general, the clearer the fingerprint artifacts, the better the estimation of the tampering mask.

III. PROBLEM FORMULATION

In this paper we tackle a counter-forensic task, aiming at hindering the capability of existing forensic detectors in spotting local forgeries applied to SAR amplitude images. We assume to have available an amplitude image \bar{I} , which has been locally manipulated for inserting or hiding details, as shown in Section II-B. Moreover, we suppose to know which is the satellite that has been used to acquire the original data and which are the acquisition mode (e.g., strip, spot, scan) and processing applied (e.g., SLC, MLC, or GRD). Notice that this situation resembles a realistic scenario, as the potential attacker typically has knowledge of the SAR system used to acquire the data under manipulation.

Our goal is deleting the manipulation artifacts from \bar{I} such that forensic detectors cannot spot the manipulation traces anymore. In doing so, we do not want to deviate from neither the semantic content nor the visual quality of \bar{I} . Moreover, we want to transfer to the attacked image the same properties of the pristine data acquired by the original SAR system, like the speckle-noise content and the traces left by the acquisition and processing operations. In other words, the final produced amplitude image must completely match the semantic characteristics of \bar{I} (i.e., it actually presents a forged area), but it has to be transparent to visual inspection (i.e., the visual quality is maintained), to SAR properties inspection, and to the forensic detector, that must estimate it being pristine in its entire area. We define the attacked amplitude image as \tilde{I} .

We consider as reference detector that proposed in [10], previously described in Section II-C, because it is specially tailored to SAR imagery and represents the state-of-the-art solution for spotting local image manipulations in the SAR field. Since this detector leverages the fingerprint extraction step as necessary operation for localizing the tampering area, our goal turns into concealing the forensic traces from \bar{I} such that its fingerprint resembles that of of pristine image.

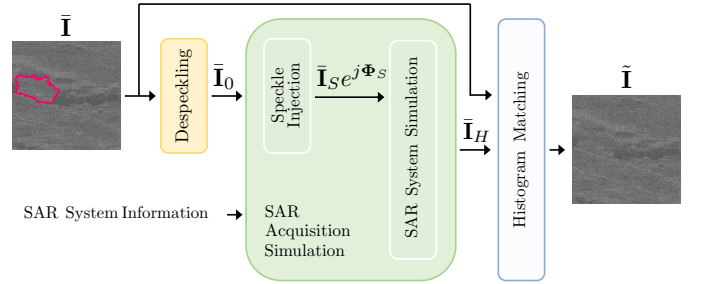


Fig. 6: Scheme of the proposed counter-forensic attack. By exploiting information on the original SAR system, we recreate the effect of a SAR acquisition through the same SAR system (or an estimate of it) used to acquire pristine data. To do so, we apply despeckling to the input manipulated image, then we simulate a re-acquisition by injecting speckle noise and filtering with the end-to-end SAR system. Finally, we match the histogram of the produced amplitude image with that of the manipulated amplitude image \bar{I} .

Fig. 5 reports the sketch of the tackled task: given a manipulated amplitude image \bar{I} , the forensic detector returns the fingerprint \bar{P} that highlights some tampering traces in correspondence of the manipulated pixels. Our proposed method leverages information on the SAR system used to acquire the original data for performing a counter-forensic attack on \bar{I} . The result is the amplitude image \tilde{I} which visually looks the same as \bar{I} and has the same SAR properties of a pristine image; however, if passed from the detector, the fingerprint \tilde{P} does not show any manipulation artifacts. We provide more details on the proposed counter-forensic attack in the next section.

IV. PROPOSED METHODOLOGY

To hide local manipulations from a SAR amplitude image \bar{I} , we propose to recreate the effect of a SAR acquisition of the scene targets depicted in \bar{I} . To do so, we exploit the original SAR system information which is available at attacker side. The output of the SAR acquisition is the amplitude image \tilde{I} , which still resembles \bar{I} from the semantic content viewpoint (both in tampered with and original areas) but presents SAR-related properties that are equivalent to those of pristine data acquired with that satellite.

A sketch of the proposed methodology is shown in Fig. 6. Our method is composed of three main steps:

- 1) *Image despeckling*. We remove the speckle noise from the manipulated amplitude image \bar{I} to recreate the noise-free scene reflectivity image as it was before acquisition.
- 2) *SAR acquisition simulation*. By leveraging information on the original SAR system, we simulate the acquisition of the targets depicted in the manipulated scene.
- 3) *Histogram matching*. We match the pixel histogram of the resulting image with that of the manipulated amplitude image \bar{I} , in order to keep the dynamic range similar to the initial one. This step can be seen as a refinement phase of the previous point.

The effect of the proposed methodology is twofold. On the one hand, by acquiring the scene targets depicted in \bar{I} with the same acquisition system of the pristine data, we force the resulting amplitude image \tilde{I} to maintain similar SAR characteristics to the pristine data, like the amount of speckle noise and its spatial and frequency pattern. The final histogram matching completes the process by adjusting the pixel dynamics. On the other hand, the SAR acquisition

processing chain acts as a counter-forensic attack that, by slightly modifying the pixel low-level information which are paramount for the detector, enables to hide the tampering traces. A detailed explanation of all the steps follows in the next lines.

A. Image Despeckling

Since the goal is reproducing the effect of a SAR acquisition of the scene targets depicted in the manipulated image, the first natural step of an attacker would be to remove the speckle noise introduced by the previous acquisition. This operation would enable to simulate the acquisition of noise-free targets, which is exactly what happens if we consider the SAR acquisition model presented before.

To do so, we leverage well-known state-of-the-art SAR despeckling algorithms, namely the Fast Adaptive Non-local SAR Despeckling (FANS) [29] and the Non-Local framework for (In)(Pol)SAR denoising (NL-SAR) [30]. Both techniques reported excellent performances on SAR data and can work with the image amplitude information alone. These characteristics make them perfectly suited for our case study with respect to modern data-driven solutions [31] that would require a specific training and work with complex images exclusively. Following a similar notation to Section II-A2, the despeckled amplitude image is defined as $\bar{\mathbf{I}}_0$.

Notice that the main disadvantage of image despeckling is the potential loss of high frequency details in the final despeckled image. As a matter of fact, the despeckling algorithm risks to remove also point scatterers that were originally depicted in the reflectivity scene. We show in our experiments that this despeckling step can be avoided, as the effects of the previous SAR acquisition are completely superseded by the new acquisition step that follows. To keep at most the frequency content of the scene depicted in the manipulated image $\bar{\mathbf{I}}$, we prove that it is a better choice to omit this step, directly going to the simulation of the SAR acquisition.

B. SAR Acquisition Simulation

This step is the main core of the proposed counter-forensic attack. It consists of recreating the acquisition of the scene targets depicted in the manipulated image by means of the same SAR system (or an estimate of it) that was used to acquire the original data. Referring to SAR background concepts reported in Section II-A, we split this step into two separate stages, namely speckle injection and SAR system simulation.

1) *Speckle Injection*: The injection of speckle noise is required to simulate the acquisition of a complex SAR image in which the targets, defined by the noise-free manipulated amplitude image $\bar{\mathbf{I}}_0$, are affected by speckle noise. To do so, we generate a complex speckle noise $\mathbf{S}e^{j\Phi_S}$ with the same size of $\bar{\mathbf{I}}_0$ and with the characteristics reported in Section II-A. In general, $\mathbf{S}(x, y) \sim \mathcal{R}(\sigma_S)$, being σ_S the scale parameter of a Rayleigh distribution, whether $\Phi_S(x, y) \sim \mathcal{U}[0, 2\pi]$.

The output image of this stage is obtained by element-wise multiplication between the input image $\bar{\mathbf{I}}_0$ and the speckle noise. This is defined as $\bar{\mathbf{I}}_S e^{j\Phi_S} = \bar{\mathbf{I}}_0 \odot \mathbf{S}e^{j\Phi_S}$, being \odot the element-wise product. Notice that the final image $\bar{\mathbf{I}}_S e^{j\Phi_S}$ is complex, i.e., it carries both amplitude and phase information.

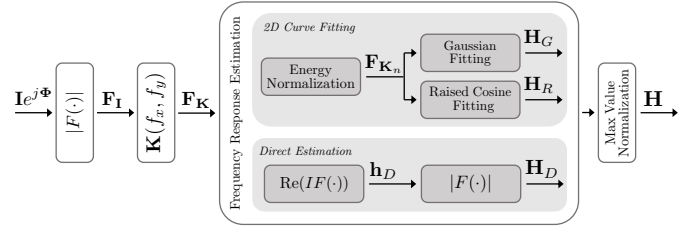


Fig. 7: Proposed pipeline for estimating the frequency response of the SAR system used to acquire $\mathbf{I}e^{j\Phi}$. The final estimated acquisition system is defined as \mathbf{H} .

Moreover, the complex image returned by this step has an extremely wide spectrum, due to the multiplication by a complex term with uniformly distributed phase in all frequencies.

2) *SAR System Simulation*: To recreate a SAR acquisition, the speckle-affected image $\bar{\mathbf{I}}_S e^{j\Phi_S}$ must be filtered through the same acquisition and processing system used to acquire the original data. This maps into the exploitation of the SAR system frequency response \mathbf{H} described in Section II-A1.

In this context, we consider four different realistic scenarios that the attacker can encounter: (i) \mathbf{H} is fully known; (ii) the attacker disposes of the original *complex* image under attack; (iii) the attacker disposes of N complex images captured by the same satellite, different from the original image under attack; (iv) the attacker only disposes of the original *amplitude* image under attack. The last three scenarios require an estimation process for extracting information on the original system frequency response. As suggested in [19], we assume the SAR system frequency response can be approximated by a real central-symmetric nonnegative function. For simplicity, we describe the proposed estimation process for case (ii), detailing the differences with respect to cases (iii) and (iv) at the end of the derivations.

To estimate \mathbf{H} , we consider four consecutive steps (see Fig. 7):

- 1) We first compute the 2D FT of the original image $\mathbf{I}e^{j\Phi}$ and take its magnitude value, defined as $\mathbf{F}_I = |F(\mathbf{I}e^{j\Phi})|$.
- 2) We apply a smoothing to \mathbf{F}_I through a Gaussian kernel \mathbf{K} . Formally, we can define the resulting magnitude spectrum as

$$\mathbf{F}_K(f_x, f_y) = \mathbf{F}_I(f_x, f_y) * \mathbf{K}(f_x, f_y), \quad (5)$$

being $*$ the 2D linear convolution and (f_x, f_y) the tuple of spatial frequencies. We do so for reducing the local variability of the acquired data. This helps untying the filter estimation process from the actual data content which is noisy and dependent on the depicted scene.

- 3) Given \mathbf{F}_K , we estimate three different versions of the frequency response of the SAR acquisition system: (i) we fit a 2D Gaussian bell; (ii) we fit a 2D Raised Cosine, as suggested in [19]; (iii) we directly estimate it by slightly modifying \mathbf{F}_K .

2D Curve Fitting. Gaussian and Raised Cosine fitting are done through the same sequence of operations. In particular, we need two further steps:

- As done in [19], we normalize $\mathbf{F}_{\mathbf{K}}$ by the square root of its energy, obtaining

$$\mathbf{F}_{\mathbf{K}_n} = \frac{\mathbf{F}_{\mathbf{K}}}{\sqrt{\sum_{f_x} \sum_{f_y} \mathbf{F}_{\mathbf{K}}^2(f_x, f_y)}}. \quad (6)$$

- Through least squares fitting, we exploit $\mathbf{F}_{\mathbf{K}_n}$ to fit a 2D Gaussian bell $\mathbf{G}(f_x, f_y)$ or a 2D raised cosine $\mathbf{R}(f_x, f_y)$. Both functions present separable components along the two frequency dimensions. $\mathbf{G}(f_z)$ is defined as

$$\mathbf{G}(f_z) = g_z \cdot e^{-\frac{(f_z - \mu_z)^2}{2\sigma_z^2}}, \quad (7)$$

where $z \in \{x, y\}$ and being g_z, μ_z and σ_z the gain, the mean value and the variance along z dimension, respectively. $\mathbf{R}(f_z)$ is defined as

$$\mathbf{R}(f_z) = (A_z - B_z \cos(\pi(f_z - f_{c_z})/f_{c_z})), f_z \leq f_{c_z}, \quad (8)$$

where f_{c_z} is the cutoff frequency ($\mathbf{R}(f_z) = 0$ for $f_z > f_{c_z}$) and $A_z > 0$ and $B_z > 0$ are model parameters [19].

We define the 2D frequency responses achieved by the least squares fitting as \mathbf{H}_G and \mathbf{H}_R , considering Gaussian and Raised Cosine, respectively. These frequency responses always correspond to real-valued central-symmetric nonnegative functions.

Direct estimation. In the last case, we directly employ $\mathbf{F}_{\mathbf{K}}$ to estimate the frequency response of the SAR acquisition filter. Notice that, being $\mathbf{F}_{\mathbf{K}}$ the frequency response of a *complex* signal, it does not necessarily correspond to a central-symmetric function. To circumvent this issue, we compute its 2D Inverse Fourier Transform (IFT) and consider only the real part contribution. Formally, we define the 2D real signal

$$\mathbf{h}_D = \text{Re}(IF(\mathbf{F}_{\mathbf{K}})), \quad (9)$$

where $IF(\cdot)$ represents the 2D Inverse Fourier transform operator. The finally estimated 2D frequency response is defined as $\mathbf{H}_D = |F(\mathbf{h}_D)|$. In this case, \mathbf{H}_D satisfies the symmetry and positivity constraints.

- 4) In the last phase, the SAR acquisition filter is estimated by normalizing the obtained frequency response, i.e., either \mathbf{H}_G , \mathbf{H}_R or \mathbf{H}_D , by its maximum value, such that all versions have maximum gain equal to 1. We denote the estimated system frequency response as \mathbf{H} . In the Gaussian case, $\mathbf{H} = \mathbf{H}_G/\mathbf{H}_{G_{\max}}$; in the Raised Cosine case, $\mathbf{H} = \mathbf{H}_R/\mathbf{H}_{R_{\max}}$; in the direct estimation case, $\mathbf{H} = \mathbf{H}_D/\mathbf{H}_{D_{\max}}$.

If the original complex image is not available at attacker side but N complex images captured by the same satellite can be found, \mathbf{H} can be estimated as the arithmetic mean of the single frequency responses estimated by each complex image.

In the case in which only the original amplitude image is known by the attacker, the estimation process is strongly affected by the loss of high frequency details in the spectrum. We show in Section VI-A that the amplitude image is not sufficiently informative for estimating the SAR system, thus returning poor results in the simulation of the re-acquisition.

C. Histogram Matching

In the last phase of the proposed attack, it may happen that the resulting amplitude image $\bar{\mathbf{I}}_H$ presents a few differences with respect to the image $\bar{\mathbf{I}}$ in terms of dynamic range and pixels' distribution. As a matter of fact, there may be little differences between the injected and the actual speckle noise distributions. Also, the estimation of the system frequency response may contain small errors. All these situations contribute to little mismatch between the distribution of attacked and non-attacked amplitude images, thus resulting in clear artifacts that may induce forensic investigators to expose the attacked ones.

To counteract this effect, we match the pixels' histogram of $\bar{\mathbf{I}}_H$ with that of the manipulated amplitude image $\bar{\mathbf{I}}$. In doing so, the dynamics and the pixel distribution are adapted to the initial ones, hindering the traces of the global operation done to hide the forgery.

We define the final amplitude image as $\tilde{\mathbf{I}}$. This image still presents the forged area, though, as we show in our experiments, the splicing area is invisible to the existing forensic detectors developed for image splicing localization.

V. EXPERIMENTAL SETUP

In this section, we describe the setup of our experimental campaign. First, we present the employed SAR image dataset; second, we provide details on the forgery creation process; third, we give information on the counter-forensic attack parameters; finally, we describe the forensic detector setup.

A. Pristine Dataset

We downloaded the data from ESA EO-CAT [32], which provides various SAR products acquired in different modes and missions. In particular, we selected the SAR Staring SpotLight (ST) Single Look Slant Range Complex (SSC) products from the TerraSAR-X ESA archive [20]; these products present a resolution of 0.25m and a 16-bit dynamic range. We purposely selected these products for three main reasons:

- They are acquired with the highest possible spatial resolution, enabling us to produce forgeries in the area of few meters.
- They are single look, meaning that the resulting SAR images are not the average of multiple satellite looks and thus present a reasonable amount of speckle noise.
- They are complex products, carrying both amplitude and phase information.

Overall, there are 24 different ST-SSC products available. The temporal coverage ranges from 2016 to 2021 and the scene content varies between city center, seaside, cropland and mountain. In particular, these products show images of four specific geographical areas, located in Rome and Dublin cities, in Gaza and in north-Italy mountains.

The size of ST-SSC products is not fixed and can be larger than $10K \times 18K$ pixels. Given the huge size of these acquisitions, we divided each of them into 1024×1024 pixels-wide images with an overlap of 512×512 pixels. This operation enables to operate at a local level with fine granularity, facilitating easy processing of the input by our networks. From each product, we extracted 400–500 complex

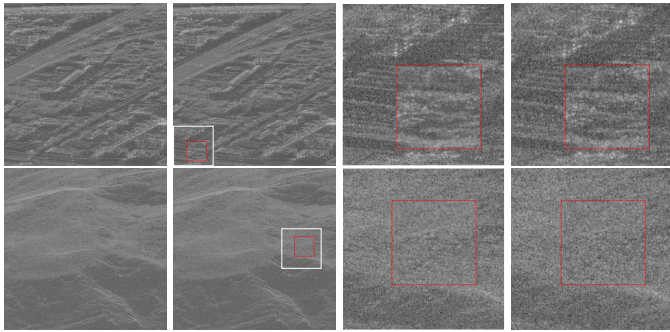


Fig. 8: Examples of the considered SAR amplitude data. First column depicts pristine images. Second column shows manipulated version of the same images; the splicing area is contained inside the red box. Third column shows a close-up of the forgery area and of the surrounding pixels (white box). Last column depicts a close-up with the proposed counter-forensic attack. Since the considered images have 16-bit dynamics, we show their amplitudes in logarithmic scale.

images, resulting in a total set of approximately $12K$ pristine data. Some examples are shown in the first column of Fig. 8¹.

B. Manipulated Dataset

To create realistic forgeries, we always considered the case in which the donor amplitude image \mathbf{I}_D and the target amplitude image \mathbf{I}_T come from the same product. This operation allows to produce realistic splicings where the difference in the dynamic range and semantic details is reasonably small, since both donor and target images belong to the original product. To run multiple experiments, we created automatic forgeries by randomly selecting donor and target regions of 128×128 pixels, as done in [10].

As done in [10], we simulated an attacker perspective by processing the donor amplitude images with post-processing operations which can make the tampering more plausible. In particular, recalling Section II-B, we applied four possible editings $E(\cdot)$ to the donor image: a Gaussian blur, an upscaling, a downscaling and a rotation. Each of the last three similarity transformations is proposed in two different versions: (i) a “Near” version, in which the similarity parameters limit the transformations to almost imperceptible changes in the edited images, like a few degree rotation; (ii) a “Far” version, in which the editing process becomes more noticeable.

In any case, all the considered editing operations do not introduce important content variations or degradations in the image visual quality. We consider this last constraint being paramount for performing realistic investigations. Indeed, we could think to include strong image perturbations like heavy noise addition or blurring. Such editing operations would carry so many artifacts that the manipulation traces could be exposed by any SAR expert looking at the image. In this scenario, there would be no reason to perform counter-forensic attacks on the manipulated images, as the image content would be so altered that any state-of-the-art detector could spot the forgery. Table I reports the parameters used for executing the editing operations. Examples of automatic forgeries with gaussian blur editing are shown in second and third column of Fig. 8¹.

¹More examples are reported in the supplemental materials.

TABLE I: Editing operations considered during the process of image local manipulation.

Editing operation	Parameters
Gaussian Blur	$\sigma = 0.5$
Upscale Near	Resize factor $\sim \mathcal{U}[1.05, 1.5)$
Upscale Far	Resize factor $\sim \mathcal{U}[1.5, 2]$
Downscale Near	Resize factor $\sim \mathcal{U}[0.65, 0.95]$
Downscale Far	Resize factor $\sim \mathcal{U}[0.5, 0.65)$
Rotate Near	Rotation angle $\sim \mathcal{U}[5, 15)$ deg
Rotate Far	Rotation angle $\sim \mathcal{U}[15, 45]$ deg

C. Counter-forensic attack parameters

1) *Image despeckling*: The two despeckling algorithms considered, i.e., FANS and NL-SAR, are both unsupervised and required no fine-tuning. We set the number of looks to 1, considering our TerraSAR-X SLC samples. For the NL-SAR, we had to process each sample as non-overlapping patches of 128×128 pixels for computational reasons. The final despeckled image is obtained by reassembling all the patches together. FANS instead worked seamlessly on the full resolution images.

2) *SAR System Frequency Response*: The 2D Gaussian kernel \mathbf{K} used for smoothing the pristine image spectrum has $\sigma = 100$ pixels and size 601×601 pixels. To fit the 2D Gaussian bell and the 2D Raised Cosine, we employed a nonlinear iterative least squares solver, whose parameters are defined in [33].

D. Detector setup

To evaluate the strength of our counter-forensic attack, we employed two different versions of the forensic detectors proposed in [10], namely the SAR Adapted Extractor (SAE) and the Augmented SAR Adapted Extractor (ASAE), which are slightly different one with the other according to the specific training pipeline employed. Specifically, the SAE detector is trained as described in Section II-C, while the ASAE detector considers data augmentation in training phase, applying upscaling to the input images to enlarge the set of available SAR products (see [10] for more details).

In our experiments, we used the detectors in the best possible conditions, i.e., we trained and tested them over a homogenous dataset, in which the same product was available both in training and testing stages. In doing so we guaranteed that, in absence of counter-forensic attacks, the detectors performed at the best of their possibilities. Indeed, we wanted to avoid the risk of introducing errors due to different data distributions in train and test stages. This methodology ensured that the unique factor which might cause a degradation in the performance is the proposed counter-forensic attack.

To train and test the forensic detectors in the best possible conditions, we always showed in training phase all the possible semantic scenarios: for each of the four considered geographical areas (Rome, Dublin, Gaza and Italy mountains), we randomly selected 70% of data for training (further split in 60 – 40% for training and validation sets, respectively) and left the remaining 30% for testing. Notice that the training images were 100% pristine, i.e., the detectors have not been trained to spot local image forgeries. Contrarily, as done in [10], the images of the test set did always present local

manipulations. This operation allows to test the detection performances in presence of tampering: if this is not the case (i.e., the test image is pristine), the detectors would report an almost flat fingerprint due to absence of inconsistencies [10]. The tampering operations were realized as explained in V-B. For each amplitude image in the test set, we considered one possible splicing area, performing on the donor image all the editing operations listed in Table I.

Following similar considerations, we stopped the detectors' pipeline at the fingerprint extraction step, i.e., we did not include the mask estimation step. The motivation is that extracting only the fingerprint and not the mask allows to reduce potential errors (with consequent performance drop) introduced during the binarization of the mask. As specified before, we put ourselves in the best possible testing conditions, in order to evaluate the amount of performance degradation cause by the suggested methodology.

VI. RESULTS

A. Quality of the attacked images

At first, we aim at evaluating the ability of our proposed counter-forensic attack in producing high-quality attacked amplitude images. As previously stated, we must produce attacked images which report similar characteristics than original pristine ones, such that an expert in the SAR field would not be able to easily spot that some global post processing operations have been applied.

To do so, we put aside for a moment the locally manipulated amplitude images, focusing only on pristine samples. For each pristine amplitude image \mathbf{I} , we generate an attacked version of it, namely $\tilde{\mathbf{I}}$, by following the methodology proposed in Section IV. Therefore, in this particular experiment, the input to the counter-forensic attack are the pristine amplitude images \mathbf{I} and not their manipulated versions $\tilde{\mathbf{I}}$. If the attacked versions of pristine samples show indistinguishable from the pristine ones, our attack can be employed to realistically modify SAR data samples that resemble original untouched ones.

Image quality metrics. As done in [12], we compare pristine and attacked samples by exploiting several similarity metrics². We evaluate the visual quality of the attacked samples by computing metrics typical of the image full-reference quality assessment field, i.e., the Structural Similarity Index Measure (SSIM) [34], and the Multi-Scale Structural Similarity Index Measure (MS-SSIM) [35]. The higher the similarity measure between attacked and pristine samples, ideally approaching 1, the better the quality of the attack, in terms of producing pixel content that visually resembles original data.

We also consider SAR compatibility metrics to evaluate our ability in reproducing speckle pattern in the attacked images. In particular, we rely on the Equivalent Number of Looks (ENL) [36], usually employed in the SAR despeckling field, to understand if the considered attacked samples are compatible with the original SAR data. The ENL is a statistical measure to quantify the level of speckle noise in SAR images. In particular, we compute the absolute relative difference of

²In the supplemental materials, we also compare attacked and pristine images for what concerns their frequency behaviour.

TABLE II: Quality metrics (SSIM / MSSIM / $|\Delta\text{-ENL}|$) between pristine amplitude images and their attacked versions in presence or absence of despeckling. We hypothesize the attacker has available the original complex image $\mathbf{I}e^{j\Phi}$ for estimating the frequency response \mathbf{H} . In bold, the best result per column.

	W/ Despeckling		W/O Despeckling
	FANS	NL-SAR	-
	SSIM / MSSIM / $ \Delta\text{-ENL} $	SSIM / MSSIM / $ \Delta\text{-ENL} $	SSIM / MSSIM / $ \Delta\text{-ENL} $
\mathbf{H}_G	0.985 / 0.997 / 306.2%	0.983 / 0.997 / 414.5%	0.991 / 0.998 / 0.518%
\mathbf{H}_R	0.984 / 0.997 / 305.2%	0.983 / 0.997 / 412.7%	0.991 / 0.998 / 0.471%
\mathbf{H}_D	0.985 / 0.997 / 305.7%	0.983 / 0.997 / 413.7%	0.991 / 0.998 / 0.458%

the ENL of attacked images with respect to their original pristine version. We define this metrics as $|\Delta\text{-ENL}|$. Our goal is achieving low values of $|\Delta\text{-ENL}|$, meaning for a realistic reproduction of speckle noise in the attacked samples.

Despeckling influence. We start evaluating the achieved similarity metrics according to presence or not of the despeckling step in our attack. To do so, we restrict our investigations to one of the four situations presented in Section IV-B2, i.e., the different levels of attacker knowledge on the SAR system frequency response \mathbf{H} . In particular, we omit the case in which \mathbf{H} is fully known, as we have no access to all the information describing the original SAR system used to capture the considered dataset. We consider the best case scenario, which reasonably consists in having available the original complex image $\mathbf{I}e^{j\Phi}$ under attack.

We consider three different estimation strategies of the SAR system frequency response, namely the Gaussian fitting, the Raised Cosine fitting and the direct estimation, leading to \mathbf{H}_G , \mathbf{H}_R and \mathbf{H}_D respectively. As regards the speckle noise injection parameters, we show results for phase-only injected speckle, as this scenario achieves far better results than cases with speckle amplitude contributions³.

The achieved results of image processing and SAR data compatibility metrics are depicted in Table II. SSIM and MS-SSIM do not show significant differences between the possible scenarios: in all situations, SSIM and MS-SSIM exceed 0.98 and 0.997 respectively, meaning for excellent visual quality. Nonetheless, omitting the despeckling step allows to achieve the best performance.

A more discriminant metrics is the $|\Delta\text{-ENL}|$. Excluding the despeckling phase reveals paramount for keeping at bay the differences in ENL between attacked and pristine images. As anticipated in Section IV-A, despeckling is removing too many high frequency details from the image under attack, including original point scatterers as well³. On the contrary, simulating a re-acquisition of the amplitude image as it is (i.e., keeping the original speckle noise) allows to reduce the ENL and renders it more similar to the pristine one. For this reason, we omit the despeckling step in all the following experiments.

Another interesting point is that the direct strategy for estimating the frequency response of the system proves to be the best option in terms of SAR data compatibility. This is worth of notice, considering that this strategy does not need the iterative least squares fitting, thus being less computation demanding.

³We report a more complete analysis in the supplemental materials.

TABLE III: Quality metrics (SSIM / MSSIM / $|\Delta\text{-ENL}|$) between pristine amplitude images and their attacked versions. In bold, the best results per column.

	Attacker availability for \mathbf{H} estimation			
	$\mathbf{I}e^{j\Phi}$ (original <i>complex</i>)	$\mathbf{I}_i e^{j\Phi_i} \neq \mathbf{I}e^{j\Phi}$	$\{\mathbf{I}_i e^{j\Phi_i}\}_{i=1}^N \neq \mathbf{I}e^{j\Phi}$ ($N = 23$)	\mathbf{I} (original <i>amplitude</i>)
	SSIM / MSSIM / $ \Delta\text{-ENL} $	SSIM / MSSIM / $ \Delta\text{-ENL} $	SSIM / MSSIM / $ \Delta\text{-ENL} $	SSIM / MSSIM / $ \Delta\text{-ENL} $
\mathbf{H}_G	0.991 / 0.998 / 0.518%	0.991 / 0.998 / 0.506%	0.991 / 0.998 / 0.519%	-
\mathbf{H}_R	0.991 / 0.998 / 0.471%	0.991 / 0.998 / 0.446%	0.991 / 0.998 / 0.449%	-
\mathbf{H}_D	0.991 / 0.998 / 0.458%	0.991 / 0.998 / 0.462%	0.991 / 0.998 / 0.462%	0.989 / 0.998 / 8.847%

Effects of the SAR system knowledge level. We now evaluate how the quality of attacked images changes according to the attacker knowledge on the original SAR system frequency response (see Section IV-B2). As done before, we omit the best knowledge case (i.e., when \mathbf{H} is fully known), but we consider four different scenarios in any case: (i) the original *complex* image $\mathbf{I}e^{j\Phi}$ under attack is available; (ii) another *complex* image $\mathbf{I}_i e^{j\Phi_i} \neq \mathbf{I}e^{j\Phi}$ captured by the same satellite is available (randomly selected from one different ST-SSC product); (iii) N *complex* images $\{\mathbf{I}_i e^{j\Phi_i}\}_{i=1}^N \neq \mathbf{I}e^{j\Phi}$ captured by the same satellite are available; in our case, we consider $N = 23$, as we dispose of 24 ST-SSC products, thus we pick one different image per product; (iv) only the original *amplitude* image \mathbf{I} under attack is available.

The achieved results are depicted in Table III³. The three different estimation strategies (i.e., \mathbf{H}_G , \mathbf{H}_R and \mathbf{H}_D) confirm to achieve very similar results among themselves. If only the original amplitude image is available, the iterative least square solver did not converge in case of \mathbf{H}_G and \mathbf{H}_R . This is due to the strongly different frequency content of the amplitude images with respect to the Gaussian and Raised Cosine functions³.

The $|\Delta\text{-ENL}|$ confirms to be the most discriminant metrics to describe the achieved image quality. The only situation which reports lower performances is that related with the original amplitude image. This was expected, as the amplitude spectrum presents much lower frequency behaviour with respect to the complex one, thus a consistent portion of high frequency details is filtered out, resulting in an increased ENL³. Interestingly, $|\Delta\text{-ENL}|$ does not change consistently if the original complex image is not available, but one or more of other complex images captured by the same satellite can be found. The achieved results lead to the conclusion that our counter-forensic attack is valid even in cases of reduced satellite information. One complex image captured by the same satellite is enough to return extremely good performances in reproducing the SAR acquisition characteristics.

Selected attack configuration. In light of the previous considerations, we omit the despeckling step and we simulate the re-acquisition by using the direct system estimation strategy with phase-only speckle injection in all the following experiments. This option allows to avoid the least squares fitting in the system frequency estimation step and to keep at bay the ENL-related artifacts on the attacked images. Moreover, to simplify the scenario, we consider having available the original complex image at attacker side, exploiting it to estimate the SAR system frequency response. As shown before, this option does not lead to limitations in the presented results.

Some examples of our attack applied into locally manipu-

lated amplitude images are shown in the last column of Fig. 8¹. Notice the subtle pattern difference between the manipulated images not passed from our counter-forensic attack (third column) and those undergone the proposed attack. This effect is noticeable especially in the splicing area, which results more realistic in terms of speckle noise in the attacked manipulated versions with respect to the manipulated-only versions. It is also worth noticing that the semantic content related to the reflectivity scene is maintained. All these characteristics make our attack a valid approach to return high quality realistic images.

B. Counter-forensic Attack Evaluation

We now evaluate the performance of the forensic detectors in presence of our proposed counter-forensic attack.

Tampering localization metrics. For each analyzed image, we evaluate the tampering localization performances by comparing the detector output fingerprint \mathbf{P} and the groundtruth tampering mask \mathbf{M} . In particular, we rely on the Area Under the Curve (AUC) of the Receiver Operating Characteristic (ROC) curve of the related binary classification problem. In absence of counter-forensic attacks, we expect the AUC of the ROC to approach 1, meaning for high detector accuracy in spotting local manipulations. Our goal is to reduce the AUC, ideally achieving 0.5, which means the detector is not anymore able to distinguish between pristine and manipulated pixels. Indeed, we want the fingerprints of attacked manipulated images to resemble those of pristine data, i.e., to be overall homogeneous in the entire pixel area⁴.

Detector results in absence of attack. To give an upper bound on the achievable detection performances, we first provide the results on the manipulated images not undergone to any counter-forensic attacks. Table IV depicts the achieved results, averaged over the test dataset, by varying the editing operation applied to the donor image.

The AUCs associated with all editing operations almost always achieve high scores, especially for the ASAE detector, which is known to be more accurate than the SAE [10]. Downscaling operations reveal challenging to expose, especially when the downscaling factor is small (i.e., “Downscale Far” editing operation). As the downscaling factor approaches 1 (i.e., “Downscale Near”), the AUC increases but still remains below the other editings. This behaviour might seem somehow unexpected, since one could think “Downscale Far” to reasonably contain more manipulation artifacts than “Downscale Near”, thus being easier to detect. Given that the main goal of this paper is not related to improving state-of-the-art detectors

⁴In the supplemental materials, we also compare the detector fingerprints of attacked manipulated and pristine images for what concerns their pixel values distribution, showing that they report similar characteristics.

TABLE IV: Average AUC in absence of counter-forensic attack. In bold, the *highest* achieved AUC per editing operation.

Detector	Editing operation						
	Gaussian Blur	Upscale Near	Upscale Far	Downscale Near	Downscale Far	Rotate Near	Rotate Far
SAE	0.933	0.941	0.947	0.829	0.681	0.924	0.918
ASAE	0.974	0.988	0.996	0.841	0.659	0.967	0.948

TABLE V: AUC in case of counter-forensic attack. First, we show the absolute AUC value, then, the relative difference with respect to the AUC in absence of attack (see Table IV). In bold, the *lowest* achieved AUC per editing operation and the maximum deviation with respect to the AUC in absence of attack. Better results are associated with lower AUCs, ideally approaching 0.5, even though AUCs $\approx 0.6/0.7$ already achieve valid performances.

Detector	Editing operation						
	Gaussian Blur	Upscale Near	Upscale Far	Downscale Near	Downscale Far	Rotate Near	Rotate Far
SAE	0.658 / -29.47%	0.678 / -27.94%	0.728 / -23.13%	0.609 / -26.54%	0.570 / -16.30%	0.648 / -29.87%	0.648 / -29.41%
ASAE	0.621 / -36.24%	0.636 / -35.63%	0.674 / -32.33%	0.586 / -30.32%	0.557 / -15.48%	0.616 / -36.30%	0.611 / -35.55%

for SAR local manipulations, we put aside investigations on the detector issues on downscaling³. This allows us to directly compare results of Table IV with those achieved in case of counter-forensic attack.

Detector results in case of attack. Table V depicts the average detection results in case of testing manipulated amplitude images undergone the proposed counter-forensic attack. It is worth noticing an important performance degradation in all scenarios. The highest achieved AUC is 0.728, in contrast with the 0.996 achieved in absence of the attack.

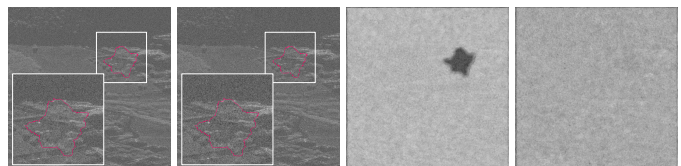
We can observe another interesting fact: the most sensitive detector to the attack is the ASAE, which is actually the best performing detector in standard situations. This implies that, if the forensic analyst is not aware of potential global attacks done to hide the manipulation area, it is quite probable that the selected detector will be the ASAE and that localization results in case of attack will be worse than those achieved by the SAE. Nonetheless, even in case of SAE detector, we report a strong performance degradation with respect to normal conditions. Apart from the ‘‘Downscale Far’’ editing which was already challenging to detect before the attack, all the editing operations undergo AUC degradation of more than 23% and 30% for SAE and ASAE detectors, respectively.

Examples of manipulated attacked images with manually made splicing and related ASAE detector fingerprints are shown in Fig. 9¹. Notice that, even in cases where the AUC is not perfectly 0.5 but instead approaches 0.65, the detector’s fingerprint is considerably less informative than the fingerprint before the attack.

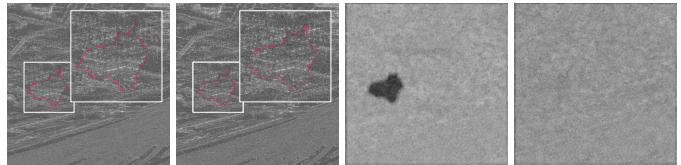
C. Realistic Attacks

In this section, we test the proposed methodology on particular cases which resemble challenging real-world attacks. Indeed, the previous analysis allows a large number of precisely controlled experiments, though squared forgery areas which have been automatically generated might be little realistic.

We consider an additional dataset including SAR data known as Moving and Stationary Target Acquisition and Recognition (MSTAR), which contains public X-band complex SAR images of military tank targets at 1 foot resolution ($\sim 30\text{cm}$) [37]. We create local manipulations by inserting target vehicles in SAR amplitude images selected from our TerraSAR-X testing dataset. Given that the average size of a

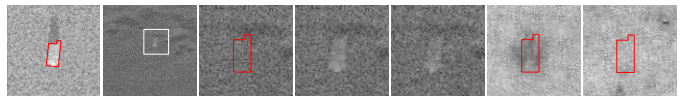


(a) The AUC before the attack is 0.991; the AUC after the attack is 0.622.

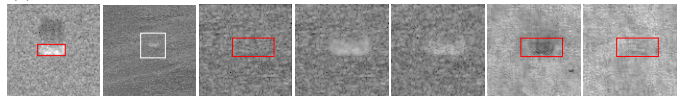


(b) The AUC before the attack is 0.984; the AUC after the attack is 0.639.

Fig. 9: Examples of the proposed counter-forensic attack applied to manipulated amplitude images. From left to right: the manipulated image in absence of counter-forensic attack; the manipulated image in presence of counter-forensic attack; the ASAE detector fingerprint in absence of counter-forensic attack; the ASAE detector fingerprint in presence of counter-forensic attack.



(a) The AUC before the attack is 0.967; the AUC after the attack is 0.545.



(b) The AUC before the attack is 0.930; the AUC after the attack is 0.599.

Fig. 10: Examples of the proposed counter-forensic attack applied to manipulated amplitude images by exploiting military vehicles selected from MSTAR dataset. From left to right: the donor SAR amplitude image of the vehicle; the manipulated image in presence of attack; close-up of the pristine image of the area inside the white box; close-up of the manipulated image in presence of attack; close-up of the ASAE detector fingerprint in absence of attack; close-up of the ASAE detector fingerprint in presence of attack.

military tank is at maximum 10×4 meters in length and width, we consider donor pixel areas around 35×16 pixels. This size is not fixed as it depends on the specific target vehicle to insert.

To create the attack, we follow the pipeline described in Section IV, including phase-only speckle noise injection and estimating the frequency response of the system directly from the available original complex image.

Some splicing examples and their related detector’s fingerprints are shown in Fig. 10¹. Notice that the attacked spliced images still carry semantic traces of the inserted vehicle: in

correspondence of the tank position, the scattered amplitude has a visible peak (see the fifth column). Despite this fact, the detector is blind to the attacked image, and its fingerprint cannot distinguish the splicing area from the surrounding pixels. This is not true for the unattacked manipulated images, in which the detector is able to expose the forged region, even if it is extremely small.

D. Why not simpler counter-forensic attacks?

In this section, we perform further experiments to validate the need of the proposed speckle injection step composing our counter-forensic pipeline. Specifically, we compare the proposed global processing operation based on speckle injection with more standard counter-forensic attacks that are usually employed to hinder forensic traces from digital images. We investigate if speckle injection is actually the best processing operation to conceal the manipulation traces. Therefore, instead of injecting a phase-only speckle noise into the manipulated amplitude images (see Section IV-B1), we pass the images to multiple different global operations alternative to speckle. After the global editing, we apply the same pipeline shown in Fig. 6: we pass each processed manipulated image through the estimated SAR end-to-end system, then we match the histogram with that of the input manipulated image.

We consider nine editing operations, listed in Table VI. In particular, the “UpDownScale” and “DownUpScale” operations consist in the application of consecutive upscaling and downscaling (or viceversa) with one resizing factor and its opposite, such to match the initial image size at the end of the processing.

Quality of the attacked images. Regarding the visual quality from natural image processing perspective (i.e., looking at SSIM and MS-SSIM), all the attacked images present extremely high quality, with results always above 0.99. This is not valid for what concerns SAR compatibility: the $|\Delta\text{-ENL}|$ assumes values similar to those achieved by speckle noise (see Table III) only in case of additive noises, while blurring or scaling operations strongly corrupt the speckle pattern of the attacked images ($|\Delta\text{-ENL}|$ is above 5% with respect to 0.45% of speckle injection)³. In the next lines, we investigate the counter-forensic strength of additive noise global processing operations. We do not include blurring or scaling operations since they do not resemble realistic attacks.

Counter-forensic attack evaluation. We report the achieved detection results on the attacked images in Table VII. For simplicity, we only consider the ASAE detector, as it demonstrated the most sensitive to counter-forensic attacks (see Table V). All the alternative global operations report extremely high AUC values, meaning for absence of counter-forensic effect. The proposed speckle injection process demonstrates the best option to hide manipulation artifacts.

E. Results’ Discussion

We believe the strength of the proposed approach lies in the exploitation of the complex nature of SAR images for hindering the manipulation traces. Indeed, the speckle injection step contributes in widening the frequency spectrum

TABLE VI: Global editing operations considered during the ablation study. \mathcal{N} , \mathcal{L} , \mathcal{P} and \mathcal{U} indicate the Gaussian, Laplace, Poisson and Uniform distributions, respectively.

Global editing operation	Parameters
Gaussian Blur	$\sigma = 0.5$
UpDownScale Near	Resize factors = $\{1.05, 1/1.05\}$
DownUpScale Near	Resize factors = $\{1/1.05, 1.05\}$
UpDownScale Far	Resize factors = $\{1.5, 1/1.5\}$
DownUpScale Far	Resize factors = $\{1/1.5, 1.5\}$
Additive Gaussian Noise	$\sim \mathcal{N}(0, 0.0005 \cdot (2^{16} - 1))$
Additive Laplacian Noise	$\sim \mathcal{L}(0, 0.0005 \cdot (2^{16} - 1))$
Additive Poisson Noise	$\sim \mathcal{P}(0.0005 \cdot (2^{16} - 1))$
Additive Uniform Noise	$\sim \mathcal{U}[-50, 50]$

of the manipulated image and conceals the subtle editing traces searched by forensic detectors. Though it is true that noise addition operations like those tested in Section VI-D are enlarging the spectrum as well, the speckle injection step is adding a complex phase term which is paramount to recreate the effect of a SAR acquisition. All the other global operations do not consider processing complex images, as they act only on the magnitude component.

The further filtering operation through the estimated end-to-end SAR system provides the correct frequency shaping to reproduce the same SAR characteristics of original pristine images. This step is also quite important for hiding local editing artifacts that would be noticeable at human inspection even after the speckle injection stage. To reproduce exactly the same pattern of the original SAR images, we have to apply the correct shaping filter corresponding to the SAR system used for pristine acquisitions³.

VII. CONCLUSIONS

In this paper, we prove that an experienced SAR practitioner can effectively conceal local manipulation traces within SAR amplitude images. By exploiting the complex nature of SAR data, our devised counter-forensic attack involves simulating a re-acquisition of the manipulated amplitude image by the same SAR system that was used to acquire its original, unaltered, complex version. Through our experimental campaign, we show how the attacker can obscure all signs of manipulation, thereby presenting the image as if it were legitimately acquired by the system.

We believe our proposed methodology holds significant advantages for the SAR forensic community for three primary reasons: first, it allows to simulate worrying scenarios in which a malicious user aims at erasing the traces of local manipulations; second, it answers the needs for privacy preservation by hiding sensitive targets; finally, it assesses the robustness of existing forensic detectors in case of adversarial attacks.

We evaluate the efficacy of the suggested counter-forensic method across a range of scenarios, analyzing different manipulation techniques. We experiment on data undergone to automatic and hand-made local manipulations, considering also the alarming scenario of military vehicles insertion. The results obtained demonstrate that our developed attack effectively eradicates any evidence of manipulation, even fooling sophisticated forensic detection systems. Moreover, the visual quality and the SAR properties of the attacked images are

TABLE VII: Average AUC achieved in presence of counter-forensic attack, for different global editing operations considered in the ablation study. In bold, the *lowest* achieved AUC per editing operation.

Global Editing	Editing operation						
	Gaussian Blur	Upscale Near	Upscale Far	Downscale Near	Downscale Far	Rotate Near	Rotate Far
Additive Gaussian	0.893	0.912	0.932	0.785	0.653	0.879	0.863
Additive Laplacian	0.849	0.865	0.886	0.755	0.655	0.835	0.823
Additive Poisson	0.902	0.923	0.945	0.787	0.649	0.888	0.870
Additive Uniform	0.908	0.928	0.947	0.794	0.653	0.894	0.877
Speckle Injection	0.621	0.636	0.674	0.586	0.557	0.616	0.611

maintained, to the extent that even an expert SAR scientist would unlikely notice the difference with the original data.

REFERENCES

- [1] C. Program, *Copernicus Open Access Hub*, Accessed January 2nd, 2022, <https://scihub.copernicus.eu/>.
- [2] ICEYE, *ICEYE SAR Datasets*, March 2023 (accessed March 22nd, 2023), <https://www.iceye.com/downloads/datasets>.
- [3] C. Space, *Capella Space Open Data Gallery*, March 2023 (accessed March 22nd, 2023), <https://www.capellaspace.com/gallery/>.
- [4] A. Moreira, P. Prats-Iraola, M. Younis, G. Krieger, I. Hajnsek, and K. P. Papathanassiou, "A tutorial on synthetic aperture radar," *IEEE Geoscience and Remote Sensing Magazine*, 2013.
- [5] A. Tsokas, M. Rysz, P. M. Pardalos, and K. Dipple, "Sar data applications in earth observation: An overview," *Expert Systems with Applications*, 2022.
- [6] R. Hummel, "Model-based atr using synthetic aperture radar," in *Record of the IEEE 2000 International Radar Conference [Cat. No. 00CH37037]*, 2000.
- [7] Y.-L. Chang, A. Anagaw, L. Chang, Y. C. Wang, C.-Y. Hsiao, and W.-H. Lee, "Ship detection based on yolov2 for sar imagery," *Remote Sensing*, 2019.
- [8] L. Chen, S. Tan, Z. Pan, J. Xing, Z. Yuan, X. Xing, and P. Zhang, "A new framework for automatic airports extraction from sar images using multi-level dual attention mechanism," *Remote Sensing*, vol. 12, 2020.
- [9] Z. Wang, Y. Li, F. Yu, W. Yu, Z. Jiang, and Y. Ding, "Object detection capability evaluation for sar image," in *2016 IEEE International Geoscience and Remote Sensing Symposium (IGARSS)*, 2016.
- [10] E. D. Cannas, N. Bonettini, S. Mandelli, P. Bestagini, and S. Tubaro, "Amplitude sar imagery splicing localization," *IEEE Access*, vol. 10, pp. 33 882–33 899, 2022.
- [11] L. Abady, E. D. Cannas, P. Bestagini, B. Tondi, S. Tubaro, and M. Barni, "An overview on the generation and detection of synthetic and manipulated satellite images," *APSIPA Transactions on Signal and Information Processing*, 2022.
- [12] E. D. Cannas, S. Mandelli, P. Bestagini, S. Tubaro, and E. J. Delp, "Deep image prior amplitude sar image anonymization," *Remote Sensing*, vol. 15, no. 15, p. 3750, 2023.
- [13] R. Bamler and B. Schättler, "Sar data acquisition and image formation," *Geocoding: ERS-1 SAR Data and Systems*, Wichmann-Verlag, pp. 53–102, 1993.
- [14] J. W. Goodman, "Some fundamental properties of speckle," *JOSA*, vol. 66, no. 11, pp. 1145–1150, 1976.
- [15] C. Oliver and S. Quegan, *Understanding synthetic aperture radar images*. SciTech Publishing, 2004.
- [16] E. ESA, *ICEYE full archive and tasking*, Accessed January 19th, 2024), <https://eocat.esa.int/eo-catalogue/concepts/platforms/bd393313-f583-5012-89f9-bf96c3c30d6c/ICEYE?httpAccept=text/html>.
- [17] I. P. Documentation, *Single Look Complex Image*, Accessed January 19th, 2024), <https://sar.iceye.com/5.0/productFormats/slc/>.
- [18] P. Guccione, A. M. Guarnieri, and M. Zonno, "Azimuth antenna maximum likelihood estimation by persistent point scatterers in sar images," *IEEE transactions on geoscience and remote sensing*, vol. 52, no. 2, pp. 947–955, 2013.
- [19] A. Lapini, T. Bianchi, F. Argenti, and L. Alparone, "Blind speckle decorrelation for sar image despeckling," *IEEE transactions on geoscience and remote sensing*, vol. 52, no. 2, pp. 1044–1058, 2013.
- [20] ESA, *TerraSAR-X ESA archive*, Accessed January 19th, 2024), <https://earth.esa.int/eogateway/catalog/terrasar-x-esa-archive>.
- [21] J. Dainty, "Some statistical properties of random speckle patterns in coherent and partially coherent illumination," *Optica Acta: International Journal of Optics*, vol. 17, no. 10, pp. 761–772, 1970.
- [22] D. Long and F. Ulaby, *Microwave radar and radiometric remote sensing*. Artech, 2015.
- [23] L. Abady, M. Barni, A. Garzelli, and B. Tondi, "GAN generation of synthetic multispectral satellite images," in *Image and Signal Processing for Remote Sensing*, 2020.
- [24] B. Zhao, S. Zhang, C. Xu, Y. Sun, and C. Deng, "Deep fake geography? when geospatial data encounter artificial intelligence," *Cartography and Geographic Information Science*, vol. 48, no. 4, pp. 338–352, 2021. [Online]. Available: <https://doi.org/10.1080/15230406.2021.1910075>
- [25] D. Cozzolino, G. Poggi, and L. Verdoliva, "Splicebuster: A new blind image splicing detector," in *IEEE International Workshop on Information Forensics and Security (WIFS)*, 2015.
- [26] D. Cozzolino and L. Verdoliva, "Noiseprint: A cnn-based camera model fingerprint," *IEEE Transactions on Information Forensics and Security*, vol. 15, pp. 144–159, 2020.
- [27] J. Lukas, J. Fridrich, and M. Goljan, "Digital camera identification from sensor pattern noise," *IEEE Transactions on Information Forensics and Security (TIFS)*, vol. 1, pp. 205–214, 2006.
- [28] K. Zhang, W. Zuo, Y. Chen, D. Meng, and L. Zhang, "Beyond a gaussian denoiser: Residual learning of deep cnn for image denoising," *IEEE Transactions on Image Processing*, vol. 26, no. 7, pp. 3142–3155, 2017.
- [29] D. Cozzolino, S. Parrilli, G. Scarpa, G. Poggi, and L. Verdoliva, "Fast adaptive nonlocal sar despeckling," *IEEE Geoscience and Remote Sensing Letters*, vol. 11, no. 2, pp. 524–528, 2013.
- [30] C.-A. Deledalle, L. Denis, F. Tupin, A. Reigber, and M. Jäger, "Nl-sar: A unified nonlocal framework for resolution-preserving (pol)(in) sar denoising," *IEEE Transactions on Geoscience and Remote Sensing*, vol. 53, no. 4, pp. 2021–2038, 2014.
- [31] A. B. Molini, D. Valsesia, G. Fracastoro, and E. Magli, "Speckle2void: Deep self-supervised sar despeckling with blind-spot convolutional neural networks," *IEEE Transactions on Geoscience and Remote Sensing*, vol. 60, pp. 1–17, 2022.
- [32] ESA, "Eo-cat," <https://eocat.esa.int/sec/#data-services-area>, Accessed September 12, 2023).
- [33] MathWorks®, *Non Linear Curve Fitting in Least Squares Sense*, Accessed September 12, 2023), <https://www.mathworks.com/help/optim/ug/lsqcurvefit.html>.
- [34] W. Zhou, B. Alan C., and L. Ligang, "Why is image quality assessment so difficult?" in *IEEE International Conference on Acoustics, Speech and Signal Processing (ICASSP)*, 2002.
- [35] W. Zhou, S. Eero P., and B. Alan C., "Multiscale structural similarity for image quality assessment," in *Asilomar Conference on Signals, Systems and Computers*, 2003.
- [36] L. Gagnon and A. Jouan, "Speckle filtering of sar images: a comparative study between complex-wavelet-based and standard filters," in *Optics & Photonics*, 1997.
- [37] T. D. Ross, S. W. Worrell, V. J. Velten, J. C. Mossing, and M. L. Bryant, "Standard sar atr evaluation experiments using the mstar public release data set," in *Algorithms for Synthetic Aperture Radar Imagery V*, vol. 3370. SPIE, 1998, pp. 566–573.